Solar wind Helium ion interaction with Mg and Fe rich pyroxene as Mercury surface analogue

Herbert Biber[a],[*], Paul S. Szabo[a], Noah Jäggi[b], Martin Wallner[a], Reinhard Stadlmayr[a], Marcos V. Moro[c], Andreas Nenning[d], Andreas Mutzke[e], Klaus Mezger[f], Helmut Lammer[g], Daniel Primetzhofer[c], Jürgen Fleig[d], André Galli[b], Peter Wurz[b], Friedrich Aumayr[a]

[a] Institute of Applied Physics, TU Wien, Wiedner Hauptstraße 8-10, 1040 Vienna, Austria
[b] Physics Institute, University of Bern, Sidlerstrasse 5, 3012 Bern, Switzerland
[c] Department of Physics and Astronomy, Uppsala University, Lägerhyddsvägen 1, 752 37 Uppsala, Sweden
[d] Institute of Chemical Technologies and Analytics, TU Wien, Getreidemarkt 9, 1060 Vienna, Austria
[e] Max Planck Institute for Plasma Physics, Wendelsteinstraße 1, 17491 Greifswald, Germany
[f] Institute of Geological Sciences, University of Bern, Baltzerstrasse 1 + 3, 3012 Bern, Switzerland
[g] Space Research Institute, Austrian Academy of Sciences, Schmiedlstraße 6, 8042 Graz, Austria

ABSTRACT

The surface of Mercury is continuously exposed to impinging solar wind ions. To improve the understanding of space weathering and exosphere formation, a detailed investigation of the ion-surface interaction is necessary. Magnesium and iron rich pyroxene $(Ca,Mg,Fe)_2[Si_2O_6]$ samples were used as analogues for Mercury's surface and irradiated with He^+ ions at solar wind energies of 4 keV. Several regimes of implantation and sputtering were observed there. The total estimated mass of implanted He coincides with the mass decrease due to He outgassing during subsequent Thermal Desorption Spectroscopy measurements. Comparison to established modeling efforts and SDTrimSP simulations show that a He saturation concentration of 10 at.% has to be assumed. A complete removal of He is observed by heating to 530 K. On the surface of Mercury, temperatures between about 100 K and 700 K are expected. This temperature will therefore influence the implantation and release of He into Mercury's exosphere.

1. Introduction

The surface of the planet Mercury is irradiated by a continuous stream of ions, emitted from the Sun. This so-called solar wind consists of 96% protons, 4% $^4He^{2+}$ and small fractions of heavier ions [1]. The solar wind has an average velocity of about 450 km/s [2], equivalent to about 1 keV/amu. Solar wind sputtering is expected to be one of the main drivers of the formation of Mercury's exosphere [3], a tenuous and collision-less atmosphere around the planet. This atmosphere forms by material ejection from the rocky surface. In addition to the sputtering contribution, also implantation and subsequent release of solar wind ions have to be considered. Properties like saturation concentration, penetration depth and diffusion in crystalline solids influence the depth profile of ions in the bulk material as well as the release of previously implanted projectiles. In the extreme case of a saturated regolith, one implanted He atom will be released for every impinging ion. This causes an increased flux into the exosphere [4]. Furthermore, the implantation

of solar wind can be responsible for modifications of the regolith. Protons for example are expected to be responsible for hydroxyl and water formation in minerals on Moon and Mercury [5]. The retention of He in silicate minerals has been investigated by Lord [6]. In that study four fluences from 6.1×10^{20} ions/m^2 to 6.1×10^{23} ions/m^2 at 1.8 keV with subsequent gas-release measurements were applied. A saturation in He retention for higher fluences was observed there, but the coarse steps in fluence and surface temperatures ranging from about 350 K to 520 K limit the interpretation of the results. A detailed examination of the fluence dependence of He implantation however has not been conducted so far. More recent research focused on sputtering by solar wind ions and its contribution to exosphere formation [7–9].

This study aims at delivering a more detailed picture of the interaction between solar wind He and a Mercury analogue pyroxene consisting of $(Ca,Mg,Fe)_2[Si_2O_6]$. For this purpose, thin pyroxene films on Quartz Crystal Microbalances were irradiated with 4 keV He^+ ions and fluences corresponding to several hundreds of years of solar wind

* Corresponding author.
  E-mail address: biber@iap.tuwien.ac.at (H. Biber).

Table 1
Composition of the pyroxene based films in atomic percent, as they were deposited onto the quartz crystals for irradiation. Results were obtained by combined RBS and ToF-E ERDA analysis [13].

H	C	O	Mg	Si	Ca	Fe
1.4 ± 0.1%	1.1 ± 0.1%	60.3 ± 0.9%	8.9 ± 0.3%	20.5 ± 0.5%	1.8 ± 0.1%	6.0 ± 0.2%

exposure. Subsequently, He release was observed with a quadrupole mass analyzer while the samples were heated up. By combining these techniques, implanted mass, saturation fluence and release temperature could be determined in-situ to get a better understanding of the interaction between the solar wind and Mercury's surface. Singly charged He ions were used for this purpose, as He^{2+} causes additional potential sputtering [8,10], which was not the focus of the study.

2. Methods

2.1. Quartz crystal microbalance measurements

For the measurements performed in this study, the Quartz Crystal Microbalance (QCM) technique was used, in which sample material is transferred onto a quartz crystal disc as a thin film. Mass depletion due to ion sputtering or mass increase caused by implantation of the projectiles can then be measured by monitoring the resonance frequency of the quartz crystal f_0. For layers of material that are thin compared to the quartz thickness, changes of f_0 are proportional to changes of the layer mass. According to the Sauerbrey equation, the proportionality factor between those frequency changes Δf and mass changes Δm is the negative quartz mass m_0 divided by f_0 [11]:

$$\frac{\Delta f}{f_0} = -\frac{\Delta m}{m_0} \Rightarrow \Delta m = -m_0 \frac{\Delta f}{f_0} \tag{1}$$

The mass changes caused by ion irradiation can be monitored with sample material deposited on the gold electrode of such a quartz crystal. The QCM used at TU Wien allows measuring the resonance frequency of the quartz during irradiation with a precision in the mHz range at a base frequency of 6 MHz. Frequency drifts are typically a few mHz per minute averaged over an hour, and below 1 mHz per minute over several hours. Therefore, real time in-situ measurements of mass changes in the sub monolayer range are possible [12].

One of the limitations of this technique is the pronounced temperature dependence of the quartz resonance frequency. It has a low gradient at room temperature and a minimum at about 410 K, where accurate measurements of small mass changes are possible. Above this temperature, however, resonance shifts of 10 Hz/K already at 430 K, and increasing shifts for higher temperatures, are present. Therefore, thermal drifts usually dominate the frequency behavior outside the two stable working points. This behavior is especially limiting Thermal Desorption Spectroscopy (TDS) measurements, as the large change of the quartz resonance frequency completely masks the frequency change due to mass loss, which therefore cannot be observed in real time during heating of the quartz. However, the total mass loss can be determined by the difference in frequency between the beginning and the end of a heating period as soon as the quartz has cooled down to room temperature again.

2.2. Thin film deposition and analysis

The samples used in this study were produced from a bulk pyroxene mineral. The material was deposited onto stress compensated quartz crystals using Pulsed Laser Deposition (PLD). This process has already been shown to reproduce the stoichiometry in the case of the pyroxenoid mineral wollastonite ($CaSiO_3$) [7]. The mineral used in this study is a pyroxene and therefore has a Si-content of 20 at.% and a high O-content of 60 at.%. The chemical composition of the produced PLD

films were deducted from combined Rutherford Backscattering Spectrometry (RBS) and coincidence Time-of-flight/Energy Elastic Recoil Detection Analysis (ToF-E ERDA) measurements, employing 2.0 MeV He^+ and 36 MeV I^{8+} as probing beams, respectively. These were carried out at Uppsala University (details of the experimental setup, as well as data analysis can be found in [13]). As results, an average O-content of 60.3 ± 0.9 at.% and a Si-content of 20.5 ± 0.5 at.% were found. Furthermore, the samples are rich in Mg (8.9 ± 0.3 at.%) and Fe (6.0 ± 0.2 at.%) and show no signs of He in the pristine sample (the constituents are presented in Table 1). The total areal density of the film was determined to be 1270×10^{15} atoms/cm^2, corresponding to a film thickness of about 139 nm when considering the density of Enstatite ($Mg_2Si_2O_6$) of 3.3 g/cm^3 [14]. Due to the fact, that the produced films are glassy, deviations from the nominal density will be present, adding some additional uncertainty to this value [15]. Nevertheless, the film thickness is in any case significantly larger than the range of 4 keV He in the pyroxene samples, calculated to be 31 nm, using the Binary Collision Approximation (BCA) code SDTrimSP (see Section 2.4 for more details) [16].

For direct comparison of the experimental data with the SDTrimSP code, flat samples are required. Surface structure can significantly alter sputtering rates due to different local angles of incidence and redeposition of sputtered material [17,18]. The samples were therefore inspected with an Atomic Force Microscope, revealing a root mean square roughness of 5.6 ± 3.5 nm. In this regime, only minor deviations from a flat surface are expected for sputtering, allowing a direct comparison between experimental observations and SDTrimSP results [19].

2.3. Ion beam setup

Helium irradiations at solar wind energies were carried out with two different ion beam setups at TU Wien. One part was performed using the Electron Cyclotron Resonance (ECR) ion source SOPHIE [20] and the setup described in [7]. The used ECR ion source allows creation of singly and multiply charged ions at fluxes that are high enough to be used for sputtering experiments. After extraction, a quadrupole magnet system is used for focusing the ion beam. A sector magnet then allows precise mass over charge separation of the ions. The ion beam is then focused into the sample chamber using electrostatic lenses. In addition, a SPECS IQE 12/38 ion gun based setup was used as well. This ion source is mostly suited for irradiations with singly charged ions, which is sufficient for the present study. Here, mass over charge separation was realized with a Wien velocity filter attached to the ion source [21].

In both setups, the filters introduce deflection of the ion beams and therefore prevent neutral particles from hitting the sample. Neutrals would otherwise cause an additional uncertainty in the measurements, since they are not registered when the ion flux is determined. The ion flux was obtained using a Faraday cup equipped with an electron suppressor and known entrance aperture size. The measured ion current divided by the aperture area then gives the ion flux on the sample. In both systems, pairs of deflection plates were applied to scan the ions over a sample area of about 7 × 7 mm^2, ensuring a homogenous irradiation of the sensitive area on the quartz. Current profiles of the ion beam were taken before and after every irradiation to monitor the ion beam stability. The ion flux impinging the sample was varied between $(36 \pm 4) \times 10^{15}$ ions/m^2/s and $(68 \pm 7) \times 10^{15}$ ions/m^2/s. If not stated otherwise, irradiations were performed at 298 ± 1 K, referred

to as room temperature.

The QCM holder was heated via an ohmic heater, which allowed reaching sample temperatures of up to 530 K. The temperature was determined with a K-type thermocouple, mounted directly to the quartz holder. To get additional information about the release of implanted material, a Pfeiffer Vacuum QME 220 Quadrupole Mass Analyzer (QMA) was attached to the vacuum chamber. Therefore, gas emitted from the sample could be monitored during TDS measurements.

2.4. Simulations with SDTrimSP

In addition to the laboratory experiments with ion beams, simulations using the program SDTrimSP [16] were performed. This BCA code allows to calculate collision cascades of ions in matter and was recently found to be able to correctly describe sputter yields for solar wind ions impaction on the pyroxenoid wollastonite [7]. In the dynamic mode of SDTrimSP, changes in sample stoichiometry due to preferential sputtering of composite materials in the surface layers, as well as changes in the implantation of impinging ions can be described. To prevent the accumulation of implanted projectiles at higher fluences to unphysical amounts around the penetration depth, the simulation of additional transport mechanisms or other suitable approaches are needed. The simplest way to do this is to artificially limit the number of implanted projectiles to a certain volume fraction without considering any real transport processes [22].

The enstatite ($Mg_2Si_2O_6$) density of 3.3 g/cm^3 was used as sample density for the simulations, as the determined composition is close to enstatite composition [14]. Following the procedure described in detail in Ref. [8], the O surface binding energy was set to 6.5 eV and the parameter controlling the model of surface binding energies *isbv* = 2 used (see [16] for details on the simulation parameters). This set of parameters was found to describe sputtering of the structurally similar wollastonite sample very well and also allows to reproduce Ar^+ sputter yields for the pyroxene-based samples used in this study.

3. Results

3.1. He irradiations

Several irradiations of Mg and Fe rich pyroxene samples with He^+ ions were performed at solar wind energy of 4 keV and under normal angle of incidence. A focus was put on determining the fluence dependence of the mass change, showing a very distinct characteristic behavior. Fig. 1 shows the mass change per incident ion over He fluence, which is proportional to the derivative of the quartz resonance frequency over time. A Savitzky-Golay filter was used to obtain this derivative from measured frequency data [23]. Surface contaminations and therefore adsorbate sputtering can alter the fluence dependence obtained in this way. All samples were consequently cleaned with 2 keV Ar^+ under an angle of 60° after installation into the UHV system, removing such contaminations from the surface. Therefore, removal of adsorbates is not expected to alter the measurements. The penetration depth of 2 keV Ar^+ under 60° is about 1.5 nm, which is removed by sputtering of 4 keV He^+ after a fluence of about 1.5×10^{21} ions/m^2. The cleaning is not expected to have an influence on the He irradiations, as the initial irradiations do not differ from later ones.

For irradiations at room temperature using 4 keV He^+, equilibrium is reached after about 2.2×10^{21} ions/m^2. In the equilibrium phase (region III in Fig. 1), as much He is released from the sample as is implanted. The constant mass loss observed in region III is therefore the net loss due to the sputtering of sample material. The fluence needed to reach saturation agrees well with results by Lord [6] for 1.8 keV He on silica based mineral samples, where between 6.1×10^{20} ions/m^2 and 6.1×10^{21} ions/m^2 were needed to reach sample saturation. Before equilibrium is reached, a mass increase is observed, which is interpreted to be the result of net implantation of He (region I). Between
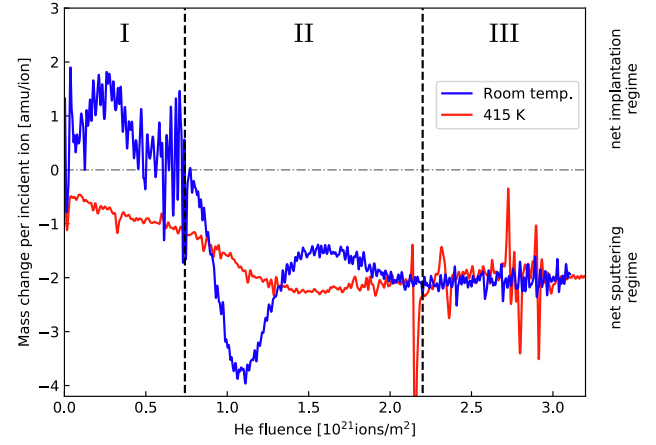

Fig. 1. Mass change per incident He^+ ion with 4 keV He^+ during the irradiation of the pyroxene coated quartz crystal at room temperature (blue) and at 415 K (red). At room temperature, a net implantation is observed until a fluence of about 0.75×10^{21} ions/m^2 (I), followed by a zone with oscillations in amplitude of net sputtering (II). After a fluence of about 2.2×10^{21} ions/m^2 an equilibrium (III) is reached and only net sputtering of the sample material is observed. For the irradiation at 415 K, no net implantation in (I), but again enhanced release in (II) was observed. Equilibrium was also reached at about 2.2×10^{21} ions/m^2 (III). (For interpretation of the references to colour in this figure legend, the reader is referred to the web version of this article.)

region I and III, a period with increased mass loss (with peaks around 1.2×10^{21} ions/m^2) followed by an interval with again reduced mass loss is measured (region II in Fig. 1). As more material seems to be ejected at the peak than in the steady state interval, more He is released from the sample than getting implanted for a given fluence range.

If constant ion current and sputter rate y (mass loss per time) are assumed, the mass of the implanted He as a function of time $R(t)$ can be calculated from the net mass change $\Delta m(t)$ measured from the beginning of the irradiation at $t = t_0$:

$$\Delta m(t) = \int_{t_0}^{t} (\dot{R}(t') - y)dt' = \int_{t_0}^{t} \dot{R}(t')dt' - y*(t - t_0) \tag{2}$$

$$\Rightarrow R(t) = \int_{t_0}^{t} \dot{R}(t')dt' = \Delta m(t) + y*(t - t_0) \tag{3}$$

When saturation is reached, the amount of He in the sample stays constant, thus $\dot{R}(t) = 0$. In this regime, the total sample mass decreases linearly with slope y. By combining this equation with the Sauerbrey Eq. (1), y can be evaluated by a fit through the saturated area of the frequency over time curve. For 4 keV He ions impacting on the pyroxene samples a mass of about 2.0 amu is removed per incident projectile. $R(t)$ is then calculated from the difference in frequency $\Delta f(t)$ minus the sputtering contribution. When applying this method for the performed irradiations, the areal mass density implanted into the samples is estimated at $(222 \pm 40) \times 10^{15}$ amu/cm^2.

In addition to the measurements at room temperature, an irradiation at 415 K (i.e., the minimum in the frequency change as function of temperature of the QCM) was performed. For these measurements, the same features, but less pronounced than at room temperature (red curve in Fig. 1) appeared at similar fluences. The difference in position of the release peak seen in Fig. 1 is within the range of scattering for measurements performed at room temperature. The implanted mass density was only $(105 \pm 22) \times 10^{15}$ amu/cm^2, but the steady state sputtering yield as well as the fluence needed to reach saturation were not affected. The less pronounced oscillations in the mass change might be caused by increased thermal diffusion at these elevated temperatures, as TDS results show an onset of He release already 20 K above room temperature (see Section 3.2).
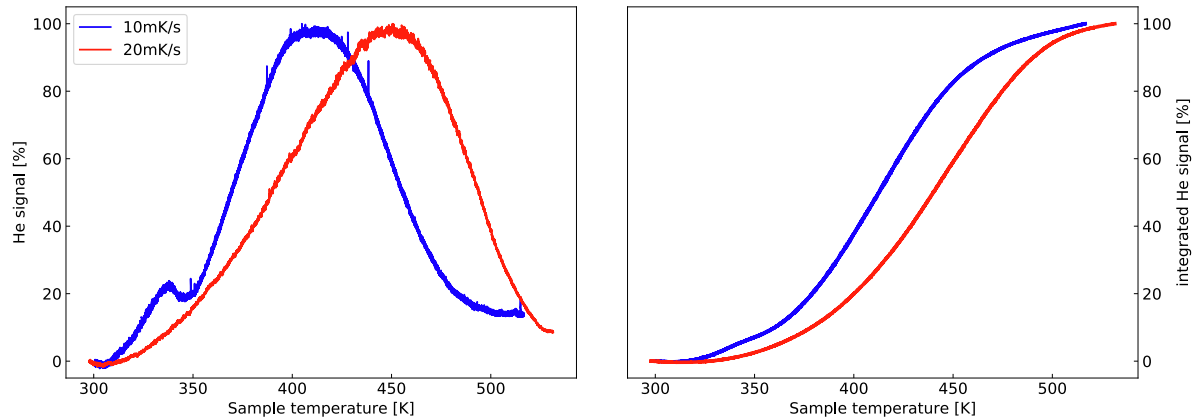
Fig. 2. He signals measured with the QMA during temperature ramps of 10 mK/s (blue curve) and 20 mK/s (red curve) on the left. The integral of the He signals are shown on the right. The sample was saturated with 4 keV He$^+$ directly before the TDS were performed. An offset for the signal background was subtracted from both signals. (For interpretation of the references to colour in this figure legend, the reader is referred to the web version of this article.)

3.2. Thermal Desorption Spectroscopy measurements

Thermal Desorption Spectroscopy (TDS) measurements were performed after the pyroxene samples were saturated with He. For this purpose, the quartz sample was heated from room temperature to 530 K with ramps of either 10 mK/s or 20 mK/s. Heating started shortly after the end of the irradiation. Frequency shifts between the end of irradiation and starting of the heating procedure were below 0.5 Hz, which is equal to 4.0×10^{15} amu/cm^2 and therefore less than 2% of the mass implanted during irradiation.

Fig. 2 shows the He signal measured with the QMA as function of the sample temperature during such measurements (left), together with the integral over the signal (right). The He signal starts to increase significantly 10–20 K above room temperature, with the peak at 411 $\pm$ 20 K for the 10 mK/s ramp and 456 $\pm$ 20 K at 20 mK/s. These results are consistent with results for the release of He implanted at 1.8 keV in forsterite by Lord [6]. In that study, the measured maximum in release is at 420 K for an irradiation fluence of 6.1×10^{20} ions/m^2 and at 440 K for a fluence of 6.1×10^{21} ions/m^2.

Measuring of the He release in real time is not possible with our present QCM setup. However, the difference in quartz frequency at room temperature before and after a heating cycle can be used to evaluate the amount of He that has been released from the sample. The average difference in mass densities is $(256 \pm 25) \times 10^{15}$ amu/cm^2, a value which very well corresponds to the amount of implanted He during irradiation (see Section 3.1).

Reference TDS measurements taken after 2 keV Ar$^+$ irradiation without He implantation resulted in mass losses of $(10–60) \times 10^{15}$ amu/cm^2. This observation is most likely related to adsorbates released from the backside of the quartz and even further improves the agreement with the amount of implanted He.

One can therefore conclude that all implanted He is released again from the sample during the heating cycle. This conclusion is supported by the fact, that irradiation of a pristine sample with He leads to the same results as measurements performed after cycles of He loading and subsequent sample heating. Heating to 530 K therefore restores the initial condition of the pyroxene films with respect to He implantation and release. However, according to SDTrimSP simulations, about 100 displacements per atom (dpa) occur when applying a fluence of 2×10^{21} He/m^2. This also indicates, that damages saturate already very early in the irradiation as well.

4. Discussion

4.1. He implantation

As described in Sections 3.1 and 3.2, He implantation in a saturated sample can be independently quantified from mass change measurements during both the irradiation phase as well as the subsequent heating phase. The implanted amount of He evaluated by the two different techniques amounts to $(222 \pm 40) \times 10^{15}$ amu/cm^2 and $(256 \pm 25) \times 10^{15}$ amu/cm^2. The detailed fluence dependence of the mass change per ion (Fig. 1), however, remains unexplained. To get more insight on this, simulations using the dynamic features of the SDTrimSP code described in Section 2.4 were performed. These simulation results are compared with the experimentally observed fluence dependence in Fig. 3.

SDTrimSP allows setting a maximum He concentration. However, the experimental results only give the total amount of implanted He, but not its concentration. Yamamura [24] investigated a similar case of retention of 4 keV He ions and found a saturation in the implanted amount, with He reaching from the surface to a depth of twice the penetration length. In the presented study, SDTrimSP simulations predict the penetration depth of 4 keV He on the investigated pyroxene to be 31 $\pm$ 1.7 nm. Assuming a similar projectile distribution in the saturated regime, the He density is calculated to 59 mg/cm^3. This is 1.8 wt% for the assumed sample density of 3.3 g/cm^3 [14] or 10 at.% with an average mass of 21.8 amu per sample atom obtained from the ion beam analysis listed in Table 1.

The dashed red curve in Fig. 3 shows a simulation without any limitation, which does not fit the experimental data at all. The calculation represented by the full red line was performed with a maximum He concentration of 10 at.%. The simulated mass change decreases sharply at a fluence of about 0.4×10^{21} ions/m^2, as He particles are starting to be removed artificially from the material by disregarding them. This fluence roughly corresponds to the position where implantation begins to decrease in the experiments. The mass change per incident ion then approaches the static SDTrimSP simulation value of -1.7 amu/ion (grey dotted line), also indicating that the effect of preferential sputtering is small. Furthermore, the additional He close to the surface hardly affects the sputtering yield. The total amount of He implanted in this scenario is 234×10^{15} amu/cm^2, which is very close to the measured value. The other option in the simulation is allowing transport due to ion bombardment. Here two mechanisms cause the transport, *damage-driven diffusion* and *pressure-driven transport*. The parameters for the strength of both effects - η_0 and K_0 - are additional parameters in the simulation, which were varied in order to match the experimental results best (see [16] for more details). With $\eta_0 = 5 \times 10^4$ and $K_0 = 100$, good agreement in the general trend and the steady state value is obtained (brown). The implanted mass of 184×10^{15} amu/cm^2 is close to the experimental value as well. The dips seen in the curve are related to simulation artefacts. These occur when comparably big amounts of He are removed from the surface layer. They however do
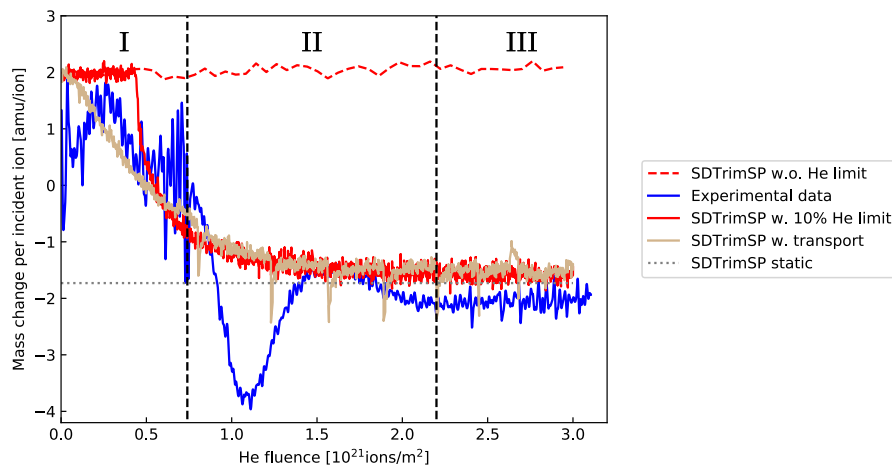
Fig. 3. Comparison of experimentally determined mass change per ion (blue curve) of a pyroxene sample, irradiated with 4 keV He$^+$ under normal incidence and results of dynamic SDTrimSP simulations. The red dashed line shows a simulation without transport and limitation of He content. For the simulation represented by the full red line, the He concentration was limited to 10%. Additionally, a calculation is shown, where transport due to ion irradiation was taken into account (brown curve). Also shown are the results of a static SDTrimSP simulation (dotted line). (For interpretation of the references to colour in this figure legend, the reader is referred to the web version of this article.)

not affect the general trend of the simulation.

Thus, both simulation approaches allowed to describe the time scales of the overall temporal evolution in mass change observed during the experiments. However, they were not able to reproduce the oscillatory mass change. Nevertheless, a He retention dependence on ion fluence quite similar to the experimentally observed one in the presented study was reported by Yamamura for 4 keV ^{3}He$^+$ on molybdenum [24]. In the simulations, Yamamura added ion-induced diffusion, thermal diffusion, trapping and reemission for projectiles to the so-called ACAT code, which is another BCA Monte Carlo code similar to SDTrimSP [25]. Although Mo and pyroxenes are quite different samples, the qualitative behavior as well as the fluence at which the oscillations take place match well. The simulations by Yamamura show, that He diffusion toward the surface is enhanced by ion impact, with a zone of increased He content leading upfront. When this front reaches the surface, enhanced He release takes place, causing the oscillatory behavior as also observed in the studied pyroxene. The He fluences at which the oscillation takes place are on the order of $(1-2) \times 10^{21}$ ions/m^2, which is comparable to the measurements presented in this study. The more sophisticated diffusion model with trapping and diffusion of detrapped projectiles in the ACAT-Diffuse code used by Yamamura [24] allows reproducing the similar oscillations in implantation of 4 keV ^{3}He$^+$ in Mo. The fact, that diffusion mechanisms are not included in SDTrimSP in such a way, could explain the differences between experimental and simulation results seen in Fig. 3, which agree well apart from the oscillations.

The effects of He irradiation were found to be consistent for different materials. For example, bubble formation was observed at similar fluences of about 10^{21} ions/m^2 in Mo [26], Al$_2$O$_3$ [27] as well as the mineral olivine (Mg,Fe)$_2$SiO$_4$ [28]. It is therefore reasonable to compare He implantation dependence on ion fluence between Mo and pyroxenes and to assume that the observations by Yamamura also hold for the presented irradiations.

4.2. Influence of He irradiations on Mercury

For the interaction between Mercury and the solar wind, both sputtering and ion implantation are of interest. For sputtering on Mercury, the solar wind composition containing mostly H and He ions and the prominent He charge state He^{2+} have to be taken into account. Due to its potential energy, He^{2+} will cause additional particle release as a result of potential sputtering [8,10]. Specifically, Szabo et al. investigated the potential sputtering of wollastonite (CaSiO$_3$) samples [8], which are similar to the samples used in the present experiments. They discuss the interplay between kinetic sputtering and potential sputtering with a solar wind composition of 96% H$^+$ and 4% ^{4}He^{2+} ions. Although the solar wind consists mainly of protons, the presence of He^{2+} ions leads to a

71% increase in sputtering compared to proton sputtering only. Their total sputtering yields for 4 keV He$^+$ under normal incidence are very close to the ones shown in this study. This indicates that the estimations made for sputtering by solar wind ions on CaSiO$_3$ are also valid for the similar pyroxene (Ca,Mg,Fe)$_2$[Si$_2$O$_6$] used in this study.

Considering the implantation of solar wind He at Mercury, it would take several hundred years to reach saturation fluences [3]. Diurnal maximum temperatures on Mercury are highly dependent on illumination, ranging from about 100 K at the nightside to 700 K in direct sunlight [29]. Depending on this temperature, the interplay of He implantation and release is very complex. For permanently cold regions, a saturation by implanted He will eventually be reached. Although also solar wind fluxes are lower in these regions, thermal diffusion is not expected to play a significant role there. In illuminated regions however, thermal He diffusion is dominant. This might lead to local variations of the He content in Mercury's exosphere, depending on solar wind flux, as well as the surface temperature. However, during the 176 days it takes for Mercury to reach the same position and orientation to the sun again, its surface is below 300 K for about half the time (see Fig. 1 in [30]). During this period, He ions impinging the surface will not be released thermally. However, the solar wind flux is also orders of magnitude too small to reach He saturation in this timespan. With temperatures exceeding the 500 K needed to remove He completely from the sample in the presented experiments, thermal release of implanted He on the dayside of Mercury is likely. Additionally, Mercury's surface is constantly processed by "gardening" [31]. Micrometeorite bombardment leads to a continuous mixing of the surface, transporting altered – and therefore also saturated – material into deeper layers and back to the surface. This way, also micro-meteorites could have an impact on the exospheres He content on the dayside.

Ultimately, several different effects can be expected to influence the He concentration in Mercury regolith. Measurements of the He content of lunar regolith, which will be affected in a similar manner, show densities far lower than the saturation concentration observed in this study [32]. However, implanted He there will be located close to the surface, while bulk sections of the grains will have lower He concentration. The He concentration observed today will of course be also influenced by historic changes in solar wind ion fluxes and the thermal environment on Mercury. A more sophisticated modelling of these effects would be needed to predict the He concentration in Hermean regolith accurately.

5. Summary and conclusion

Quartz Crystal Microbalances coated with thin films from Mg and Fe rich pyroxene mineral were irradiated with 4 keV He$^+$ under normal

incidence. With this technique, a very distinct behavior in the mass change per incident ion was measured until an equilibrium between implanted and released He is reached at a fluence of about 2.2×10^{21} ions/m^2. Thermal Desorption Spectroscopy measurements of previously He saturated samples revealed that the implanted He is released at temperatures below ~500 K. The total mass loss recorded by the QCM during TDS quantitatively agrees with the amount of previously implanted He. Simulations with the dynamic feature of the SDTrimSP code describe the general trend and time scales of the mass change observed during the experiment, using the built-in approximations for different transport mechanisms. Oscillations assumed to be due to He retention, as seen in the experiment, could not be reproduced by the simulations and need further investigation. However, simulations performed with the ACAT code by Yamamura show a very similar behavior for 4 keV ^{3}He on Mo.

On Mercury, both irradiation with solar wind ions as well as variations in temperature take place. These variations are in a regime, where the thermal mobility of implanted He is heavily affected for the samples used in this study. Timescales however are very different, as fluxes were in the order of 10^{16} ions/m^2/s in the experiments and are about 10^{11} ions/m^2/s on Mercury [3]. A full thermal cycle on Mercury takes 176 days. Additional effects like gardening of the surface can lead to He accumulation in the near surface region, as implanted He is unlikely to desorb thermally on the nightside and can be transported downwards during this period. A full model taking all these effects into account could give insight into the evolution and the present concentration of He in the regolith of Mercury.

Declaration of Competing Interest

The authors declare that they have no known competing financial interests or personal relationships that could have appeared to influence the work reported in this paper.

Acknowledgments

References

[1] S.J. Bame, J.R. Asbridge, W.C. Feldman, M.D. Montgomery, P.D. Kearney, Solar wind heavy ion abundances, Sol. Phys. 43 (2) (1975) 463–473.

[2] U. Feldman, On the sources of fast and slow solar wind, J. Geophys. Res. 110 (A7) (2005), https://doi.org/10.1029/2004JA010918.

[3] P. Wurz, J.A. Whitby, U. Rohner, J.A. Martín-Fernández, H. Lammer, C. Kolb, Self-consistent modelling of Mercury's exosphere by sputtering, micro-meteorite impact and photon-stimulated desorption, Planet. Space Sci. 58 (12) (2010) 1599–1616.

[4] R.E. Hartle, S.A. Curtis, G.E. Thomas, Mercury's helium exosphere, J. Geo. Res. Space Phys. 80 (25) (1975) 3689–3692.

[5] C. Zhu, P.B. Crandall, J.J. Gillis-Davis, H.A. Ishii, J.P. Bradley, et al., Untangling the formation and liberation of water in the lunar regolith, Proc. Natl. Acad. Sci. U.S.A. 116 (23) (2019) 11165–11170.

[6] H.C. Lord, Hydrogen and helium ion implantation into olivine and enstatite: retention coefficients, saturation concentrations, and temperature-release profiles, J. Geophys. Res. 73 (16) (1968) 5271–5280.

[7] P.S. Szabo, R. Chiba, H. Biber, R. Stadlmayr, B.M. Berger, D. Mayer, A. Mutzke, M. Doppler, M. Sauer, J. Appenroth, J. Fleig, A. Foelske-Schmitz, H. Hutter, K. Mezger, H. Lammer, A. Galli, P. Wurz, F. Aumayr, Solar wind sputtering of wollastonite as a lunar analogue material – Comparisons between experiments and simulations, Icarus 314 (2018) 98–105.

[8] P.S. Szabo, H. Biber, N. Jäggi, M. Brenner, D. Weichselbaum, et al., Dynamic potential sputtering of lunar analog material by solar wind ions, Astrophys. J. 891 (2020) 100.

[9] H. Hijazi, M.E. Bannister, H.M. Meyer III, C.M. Rouleau, F.W. Meyer, Kinetic and potential sputtering of an anorthite-like glassy thin film, J. Geophys. Res. E 122 (7) (2017) 1597–1609.

[10] F. Aumayr, H.P. Winter, Potential sputtering, Philos. Trans. R. Soc. A 362 (1814) (2004) 77–102.

[11] G. Sauerbrey, Verwendung von Schwingquarzen zur Wägung dünner Schichten und zur Mikrowägung, Z. Phys. 155 (2) (1959) 206–222.

[12] G. Hayderer, M. Schmid, P. Varga, H.P. Winter, F. Aumayr, A highly sensitive quartz-crystal microbalance for sputtering investigations in slow ion-surface collisions, Rev. Sci. Instrum. 70 (9) (1999) 3696–3700.

[13] M.V. Moro, R. Holeňák, L.Z. Medina, U. Jansson, D. Primetzhofer, Accurate high-resolution depth profiling of magnetron sputtered transition metal alloy films containing light species: a multi-method approach, Thin Solid Films 686 (2019) 137416.

[14] K.W. Bladh, R.A. Bideaux, E. Anthony-Morton, B.G. Nichols, Handbook of mineralogy, Mineralogical Society of America, Berkeley, 2001.

[15] C. Sanchez-Valle, J.D. Bass, Elasticity and pressure-induced structural changes in vitreous MgSiO3-enstatite to lower mantle pressures, Earth Planet. Sci. Lett. 295 (3-4) (2010) 523–530.

[16] A. Mutzke, R. Schneider, W. Eckstein, R. Dohmen, K. Schmid, U. Von Toussaint, G. Badelow, "SDTrimSP Version 6.00," IPP report, 2019.

[17] R. Stadlmayr, P.S. Szabo, B.M. Berger, C. Cupak, R. Chiba, D. Blöch, D. Mayer, B. Stechauner, M. Sauer, A. Foelske-Schmitz, M. Oberkofler, T. Schwarz-Selinger, A. Mutzke, F. Aumayr, Fluence dependent changes of surface morphology and sputtering yield of iron: comparison of experiments with SDTrimSP-2D, Nucl. Instrum. Methods Phys. Res. Sect. B Beam Interact. Mater. Atoms 430 (2018) 42–46.

[18] M. Küstner, W. Eckstein, V. Dose, J. Roth, The influence of surface roughness on the angular dependence of the sputter yield, Nucl. Instrum. Methods Phys. Res. Sect. B Beam Interact. Mater. Atoms 145 (3) (1998) 320–331.

[19] U. Von Toussaint, A. Mutzke, A. Manhard, Sputtering of rough surfaces: a 3D simulation study, Phys. Scr. 170 (2017) 014056.

[20] E. Galutschek, R. Trassl, E. Salzborn, F. Aumayr, H.p. Winter, Compact 14.5 GHz all-permanent magnet ECRIS for experiments with slow multicharged ions, J. Phys.: Conf. Ser. 58 (2007) 395–398.

[21] R. Stadlmayr, P.S. Szabo, D. Mayer, C. Cupak, W. Möller, F. Aumayr, Erosion of iron-tungsten model films by deuterium ion irradiation: a benchmark for TRI3DYN, Phys. Scr. T171 (2020) 014021, https://doi.org/10.1088/1402-4896/ab438f.

[22] A. Mutzke, W. Eckstein, Ion fluence dependence of the Si sputtering yield by noble gas ion bombardment, Nucl. Instrum. Methods Phys. Res. Sect. B Beam Interaction. Mater. Atoms 266 (6) (2008) 872–876.

[23] A. Savitzky, M.J. Golay, Smoothing and differentiation of data by simplified least squares procedures, Anal. Chem. 36 (8) (1964) 1627–1639.

[24] Y. Yamamura, Computer studies of reemission and depth profiles for helium on molybdenum, Nucl. Instrum. Methods Phys. Res. Sect. B Beam Interact. Mater. Atoms 28 (1) (1987) 17–26.

[25] W. Takeuchi, Y. Yamamura, Computer studies of the energy spectra and reflection coefficients of light ions, Radiat. Effects 71 (1-2) (1983) 53–64.

[26] D.J. Mazey, B.L. Eyre, J.H. Evans, S.K. Erents, G.M. McCracken, A transmission electron microscopy study of molybdenum irradiated with helium ions, J. Nucl. Mater. 64 (1-2) (1977) 145–156.

[27] N. Sasajima, T. Matsui, S. Furuno, K. Hojou, H. Otsu, Damage accumulation in Al2O3 during H2+ or He+ ion irradiation, Nucl. Instrum. Methods Phys. Res. Sect. B Beam Interact. Mater. Atoms 148 (1-4) (1999) 745–751.

[28] P. Carrez, K. Demyk, P. Cordier, L. Gengembre, J. Grimblot, et al., Low-energy helium ion irradiation-induced amorphization and chemical changes in olivine: Insights for silicate dust evolution in the interstellar medium, Meteorit. Planet. Sci. 37 (11) (2002) 1599–1614.

[29] A.R. Vasavada, D.A. Paige, S.E. Wood, Near-surface temperatures on Mercury and the Moon and the stability of polar ice deposits, Icarus 141 (2) (1999) 179–193.

[30] S.A. Curtis, R.E. Hartle, Mercury's helium exosphere after mariner 10's third encounter, J. Geo. Res. Space Phys. 83 (A4) (1978) 1551–1577.

[31] D.L. Domingue, C.R. Chapman, R.M. Killen, T.H. Zurbuchen, J.A. Gilbert, M. Sarantos, M. Benna, J.A. Slavin, D. Schriver, P.M. Trávníček, T.M. Orlando, A.L. Sprague, D.T. Blewett, J.J. Gillis-Davis, W.C. Feldman, D.J. Lawrence, G.C. Ho, D.S. Ebel, L.R. Nittler, F. Vilas, C.M. Pieters, S.C. Solomon, C.L. Johnson, R.M. Winslow, J. Helbert, P.N. Peplowski, S.Z. Weider, N. Mouawad, N.R. Izenberg, W.E. McClintock, Mercury's weather-beaten surface: understanding mercury in the context of lunar and asteroidal space weathering studies, Space Sci Rev 181 (1-4) (2014) 121–214.

[32] L. Schultz, H.W. Weber, B. Spettel, H. Hinterberger, H. Wänke, Noble gas and element distribution in agglutinate and bulk grain size fractions of soil 15601, Proc. Lunar Sci. Conf. 8 (1977) 2799–2815.